


---

This is the **accepted version** of the journal article:

Chen, Kai; Chung, Feng-Ju; Lin, Yen-Ling; [et al.]. «Metal- and Alloy-Based Core-Shell Particles in Nitrate Senary Salt with Low Thermal Hysteresis for Solar Thermal Energy Storage». ACS Applied Energy Materials, Vol. 5, Num. 3 (February 2022), p. 2697-2705. DOI 10.1021/acsaem.1c02919

---

This version is available at <https://ddd.uab.cat/record/290410>

under the terms of the  <sup>IN</sup> COPYRIGHT license

# Metal and Alloy-Based Core-Shell Particles in Nitrate Senary Salt with Low Thermal Hysteresis for Solar Thermal Energy Storage

Kai Chen (a), Feng-Ju Chung(a), Yen-Ling Lin(a), Yen-Ta Lee (b), María del Rocío Rodríguez-Laguna,(c) Arumugam Manikandan(d), Ming-Chang Lu(e),\* and Yu-Lun Chueh (d,f)\*

(a) Department of Materials Science and Engineering and Frontier Research Center on Fundamental and Applied Sciences of Matters, National Tsing Hua University, Hsinchu 30013, Taiwan

(b) Department of Mechanical Engineering, National Chiao Tung University, Hsinchu 30013, Taiwan

(c) Catalan Institute of Nanoscience and Nanotechnology (ICN2), CSIC and BIST, Campus UAB, Bellaterra, 08193 Barcelona, Spain

(d) Department of Materials Science and Engineering and Frontier Research Center on Fundamental and Applied Sciences of Matters, National Tsing Hua University, Hsinchu 30013, Taiwan.

(e) Department of Mechanical Engineering, National Taiwan University, Taipei 10617, Taiwan

(f) Department of Physics, National Sun Yat-Sen University, Kaohsiung 80424, Taiwan

\*Email: [mingchanglu@ntu.edu.tw](mailto:mingchanglu@ntu.edu.tw) \*Email: [ylochueh@mx.nthu.edu.tw](mailto:ylochueh@mx.nthu.edu.tw)

**ABSTRACT:** In this work, the microencapsulated phase change materials, Sn/ amorphous-carbon (Sn/a-C), and SnBi/amorphous carbon (SnBi/a-C) micro- particles (MPs) were successfully synthesized. The thermal stabilities of Sn/a-C and SnBi/a-C core-shell MPs were verified by cycling tests, and stable latent heats of 56 and 45.7 J/g were obtained for Sn/a-C and SnBi/a-C MPs, respectively. Compared to the high melting point of 231 °C and large thermal hysteresis (TH) of ~106 °C for the Sn/a-C MPs, the SnBi/a-C MPs exhibited a lower melting point of 125 °C and a smaller TH of 20 °C. The nitrate senary salt with a lower melting point of ~75 °C than that of the commercial HITEC salt (melting point of ~142 °C) was also synthesized to enlarge the working temperature range of the working fluid in a solar thermal power plant and to demonstrate the latent heat-enhanced thermal energy storage using the SnBi/a-C MPs. The heat capacity can be enhanced by 200% by doping with 20 wt % Sn/a-C MPs into the HITEC salt, and it can be enhanced by 734% by doping with 20 wt % SnBi/a-C MPs into the senary salt. In addition, the viscosities of the HITEC salt and senary salt doped with the Sn/a-C and SnBi/a-C MPs were not appreciably raised by doping with the MPs. The various approaches accomplished in this work demonstrate (1) enhancing heat capacity of the working fluid by exploiting the latent heats of the embedded MPs; (2) lowering the TH of the MPs by using the alloy metal particles; and (3) extending the working temperature range by synthesizing the senary salt. These approaches could be applied for enhancing energy storage in solar thermal power plants and facilitating waste heat recovery.

**KEYWORDS:** Sn/amorphous-carbon microparticles, SnBi/amorphous-carbon microparticles, latent heat, solar-thermal energy storage, thermal hysteresis, viscosity, HITEC salt, senary salt

## 1. INTRODUCTION

Human society relies heavily on fossil fuels, with more than 60% of the world's electricity generation in 2020 being from fossil fuels.<sup>1</sup> The burning of fossil fuels results in a large amount of carbon dioxide and deteriorates the greenhouse effect.<sup>2</sup> The greenhouse effect raises the global temperature and leads to dangerous climate changes.<sup>3,4</sup> Scientists have been dedicated to finding alternative energy sources to mitigate climate change. Solar energy is a promising renewable energy resource due to its abundance, non-toxic, and diverse applications.<sup>5</sup> The conversion of solar energy into electricity can be achieved by two major techniques: photovoltaics and solar thermal power plants. Photovoltaics is the direct method of conversion; however, the high cost of solar panels and limited efficiency hinder its usage. In a solar thermal power plant, solar energy can be stored as thermal energy and converted into electricity when power is needed. A solar thermal power plant, which has a heat-to-electricity energy conversion efficiency of up to 50%, is more efficient than photovoltaics.<sup>6,7</sup> However, the thermal energy storage in solar thermal power plants is limited by the heat capacity of the working fluid.<sup>8</sup> Nevertheless, the enhancement of thermal energy storage by exploiting the latent heats of the embedded encapsulated micro/nanoparticles in the working fluids has been demonstrated.<sup>9</sup> Molten salts are generally used as the working fluids in solar thermal power plants and they typically have an up-limit operating temperature range between 450 and 500 °C.<sup>10–12</sup> The utilization of molten salt as the working fluid can generate a steam at a high temperature above 450 °C and gives an energy conversion efficiency of 40% of the solar thermal power plants.<sup>13,14</sup> Besides, adding phase-change materials (PCMs) in the molten salt has been proven to be an effective way to enhance thermal energy storage in the past.<sup>15–18</sup> The PCMs have the ability to store and release thermal energy in the form of latent heat.<sup>19</sup> This feature enhances the energy storage performance of solar thermal plants. In the literature, low-temperature PCMs have been investigated and developed for many years for building applications.<sup>20</sup> However, PCMs for medium and high temperatures ( $\geq 100$  °C) have not caught much attention so far.<sup>21</sup> High-temperature PCMs can be applied to enhance energy storage in solar cooling systems<sup>22</sup> and waste heat recovery systems.<sup>23</sup> Nonetheless, PCMs doped into the working fluids in the power plant may leak out, leading to the formation of contamination during the phase-change process. Thus, encapsulation of the PCMs to prevent leakage into the working fluid is crucial. Our research group has been working on the material engineering of encapsulation of the PCMs. The controllability of latent heat absorption/release in a certain temperature range for the PCMs has been demonstrated.<sup>17</sup>

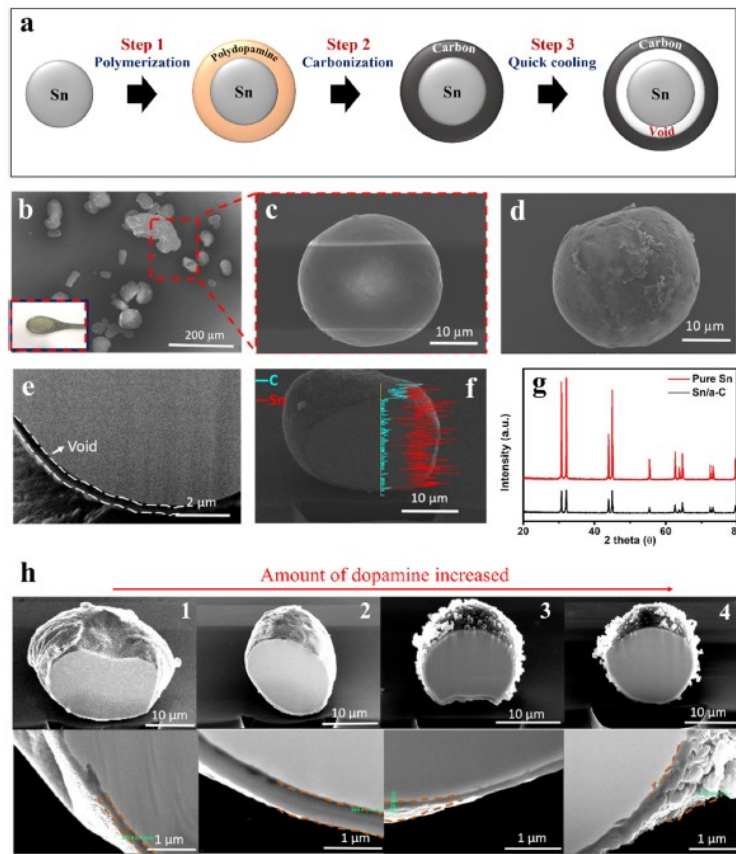


Figure 1. (a) Schematic illustration of the process of amorphous carbon coating on Sn MPs, (b) SEM image of the pure Sn MPs. The insert is a picture of the pure Sn MPs. (c) A high magnification SEM image of the pure Sn MPs was taken from (b). (d) A SEM image of Sn/a-C MPs. (e) A SEM image of FIB cross-section region at the edge to show void between core and shell. (f) An EDX line scan mapping image of C and Sn, (g) XRD spectra of pure Sn and Sn/a-C MPs. (h) A FIB cross-section SEM image of Sn/a-C MPs for different amount of dopamine 25 (h-1), 50 (h-2), 75 (h-3), and 150 mg (h-4).

Moreover, we also show that a eutectic salt doped with the Sn/ SiO<sub>x</sub> core-shell nanoparticles gives enhanced solar thermal energy storage by releasing the latent heat of the particles.<sup>15</sup> In addition, the factors causing the thermal hysteresis (TH) are identified.<sup>24–27</sup>

In this work, tin (Sn) was chosen as the doping material because its latent heat can contribute at a melting temperature of 225 °C, which is in the working temperature range of a solar thermal power plant. Besides, it has both a high thermal conductivity of 66.8 W/m K and a large latent heat of 7.03 kJ per mole. The amorphous carbon shell layer is applied to encapsulate the Sn microparticles (MPs) to prevent oxidation and fusion with the existing molten salt during the hightemperature thermal cyclic processes. Furthermore, to achieve a large thermal storage performance and to further reduce the TH. Two kinds of Sn encapsulation with amorphous carbon MPs (Sn/a-C MPs) were synthesized: core-shell and yolk-shell Sn/a-C MPs. The yolk-shell structure, which is a special kind of the core-shell structure, consists of the core MPs, a void layer between the core MPs, and the shell layer. The void between the core and the shell layer can accommodate the volume expansion and contraction of the MPs during the phase-change process. Additionally, the thermal stability of Sn/ a-C MPs was examined by a thermal cycling test.

The results showed that the Sn/a-C MPs exhibited a stable latent heat of  $\sim 56$  J/g. Moreover, by coating the bismuth (Bi) metal layer through the chemical reduction on the pure Sn MPs, the SnBi/a-C MPs were synthesized. Compared to the TH of  $\sim 106$  °C and melting point of 231 °C for the Sn/a-C MPs, the SnBi/a-C MPs successfully reduced the TH to 20 °C with a lower melting point of 142 °C. In addition, a senary nitride salt that can be operated at a lower temperature was also synthesized. The heat capacity was enhanced by 200% by doping 20 wt % Sn/a-C MPs into the HITEC salt, and it was enhanced by 734% by doping 20 wt % SnBi/a-C MPs into the senary salt. Furthermore, the viscosities of the molten salts doped with the MPs were also examined. It was found that the viscosities of the molten salts were not significantly altered by the doping particles. The demonstrated enhanced heat capacities of the molten salts using the latent heat of the MPs and lower TH using the alloy MPs can be applied to enhance energy storage in solar thermal power plants and various energy storage systems.

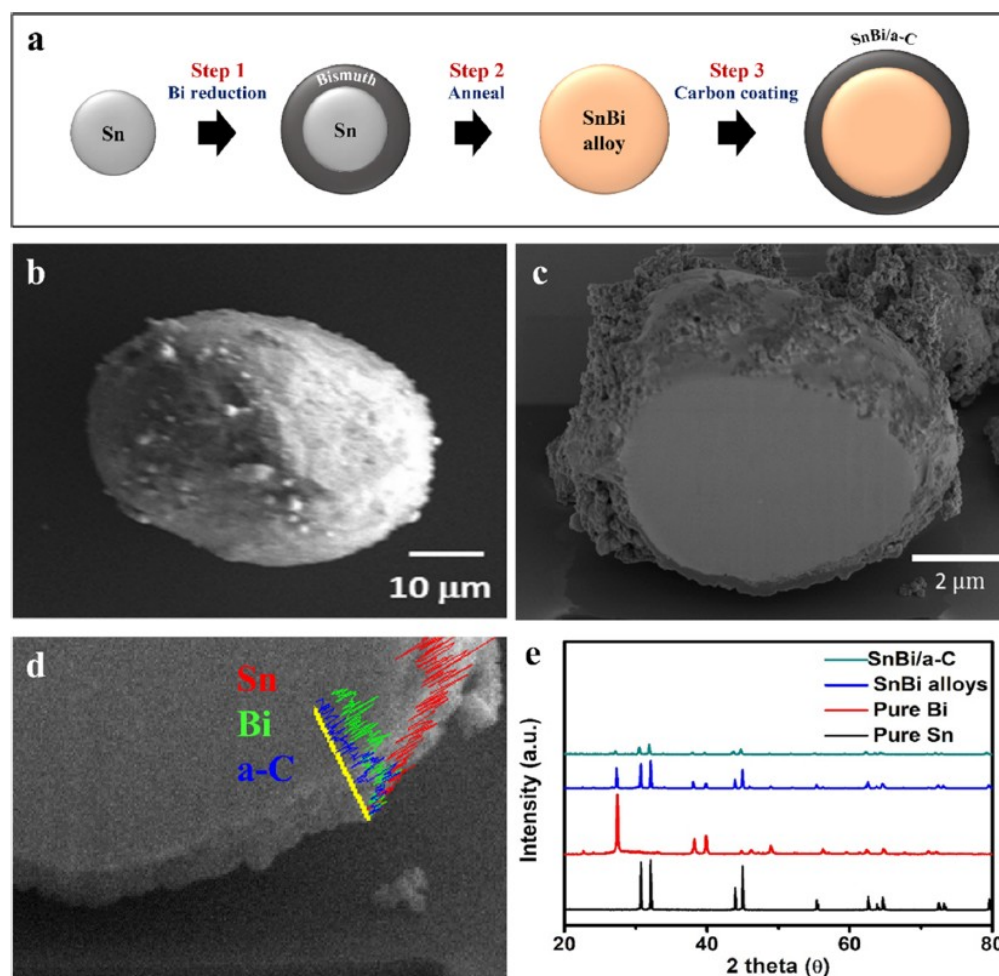


Figure 2. (a) Schematic illustration of the process of amorphous carbon coating on SnBi MPs, (b) A SEM image of the pure SnBi/a-C MPs, and (c) A FIB cross-section image (d) An EDX line scan mapping image of Bi, a-C and Sn, (e) XRD spectra of pure Sn, Bi, SnBi alloy, and SnBi/a-C MPs

## 2. EXPERIMENTAL SECTION

### 2.1. Synthesis of Sn/Amorphous Carbon (a-C) Core-Shell MPs.

The as-received Sn MPs [Sigma-Aldrich Co., purity: 99.75%] were coated with amorphous carbon via self-polymerization with dopamine as the precursor as illustrated in [Figure 1a](#). Initially, 0.0605 g of Tris base was added into 50 mL of deionized (DI) water and several drops of 35 wt % HCl aqueous solution was added into the solution to control a pH of 8.5. Then, 0.2 g of Sn MPs were dispersed into solution, followed by magnetic stirring at 700 rpm for 2 h. Subsequently, to control the thickness of the amorphous carbon layer, the amount of dopamine was varied from 0.025 to 0.15 g and they were added into the solution separately for self-polymerization at the alkaline environment to form Sn/polydopamine. The solution was stirred continuously for 16 h at 750 rpm. After the polymerization process, the MPs were filtered out, washed with DI water and ethanol three times to get rid of residual impurities. They were then dried at 60 °C for 24 h in a vacuum oven. Finally, the dried core-shell particles were annealed in a furnace at a heating rate of 20 °C/min to 500 °C for 2 h. The core-shell and yolk-shell MPs were obtained by adjusting the cooling rate in the furnace.

### 2.2. Synthesis of SnBi/Amorphous Carbon (a-C) Core-Shell MPs.

Bismuth nitrate pentahydrate [Sigma-Aldrich Co., purity: 99.99%] as a precursor of bismuth and sodium borohydride [Sigma-Aldrich Co., purity: 98%] as a reductant were used to prepare the SnBi alloy MPs by the chemical reduction method as shown in [Figure 2a](#). At first, 0.2 g of Sn MPs was dispersed into 50 mL of DI water at 5 °C. The low-temperature condition can slow down the reduction rate to avoid the nucleation effect. Then, 0.11 g of sodium borohydride powder was added to the solution with magnetic stirring of 150 rpm. Afterward, 0.12 g of bismuth nitrate pentahydrate was added to the mixture/solution. Then, Sn/Bi particles were filtered out, washed with acetone, centrifuged, and dried in a vacuum oven at 80 °C. Finally, the dried particles were annealed at 400 °C in N<sub>2</sub> atmosphere and re-dispersed for further a-C coating. The as-prepared SnBi alloy particles were coated by amorphous carbon via self-polymerization process, they were then annealed to form the shell coating on the MPs

### 2.3. Material characterization.

Surface morphologies, particle size, and the microstructure of the particles were examined by field-emission scanning electron microscopy (FE-SEM, Hitachi SU-8010).

The crystalline structure of pure Sn, pure Bi, SnBi alloy, Sn/a-C, and SnBi/a-C particles were confirmed by the X-ray diffractometer (XRD) D2 phasor. A focused ion beam (FIB) system (SMI 3050) was used to prepare the hemispherical sample for the observation of the cross-sectional structure and the shell thickness of the carbon layer-coated Sn MPs. Line scan mode of energy-dispersive X-ray spectroscopy (EDX) was used to confirm the formation of the carbon shell on the Sn MPs. The phase-change behavior of the Sn/a-C and SnBi/a-C MPs were also investigated, including the measurements of latent heat and heat capacity, by a modulated differential scanning calorimeter (DSC 1. STARE System, Mettler Toledo) with an analysis method following the ASTM (American Society for Testing and Materials) standard (ASTM 1269-11). The viscosities of molten salts doped with the Sn/a-C and SnBi/a-C MPs were also measured by using a programmable viscometer (DV3TLV, Brookfield Engineering Lab. Inc.) equipped with a cylindrical spindle (sc4 34).

### 3. RESULTS AND DISCUSSION

The Sn/a-C core-shell and yolk-shell MPs were synthesized on as-received Sn MPs by the self-polymerization process with dopamine followed by annealing and cooling process (see Method Section for detail process). Figure 1b,c is the SEM image of as-received Sn MPs, showing smooth surfaces. The Sn MPs have an average particle size of 18.6  $\mu\text{m}$  (Figure S1a). Note that the Sn/a-C MPs can be mass-produced as shown in the inset of Figure 1b. The surface of pure Sn MPs became rough after the coating of an a-C layer as shown in Figure 1d. In addition, the void between the core material and shell layer is observed by performing FIB analysis as shown in Figure 1e, confirming the yolk-shell structure of Sn/a-C MPs. The presence of a void between the core and the shell materials could act as a buffering space for the volume expansion of the Sn core, which decreases the stress during the phase-change process. Moreover, the average particle size of Sn/a-C MPs increased from 18.6  $\mu\text{m}$  for the pure Sn MPs to 25.4  $\mu\text{m}$  for the Sn/a-C MP (Figure S1b). In addition, the EDX line scan confirms the strong signals of Sn from the core and C from the shell layers (Figure 1f), suggesting the core-shell structure of the MPs. The XRD spectra of both Sn and Sn/a-C MPs as shown in Figure 1g exhibits crystalline Sn peaks, confirming the amorphous structure of the carbon shell layer. The thickness of the carbon shell layer can be well controlled by varying the amount of dopamine during the synthesis process. With the amounts of dopamine of 25, 50, 75, and 150 mg, the obtained shell thicknesses were 430, 540, 612, and 1300 nm as shown in Figure 1, respectively. The shell thickness and the roughness increased with the increase in the amount of dopamine.

To reduce the TH of the Sn/a-C MPs, we synthesized the SnBi/a-C MPs by coating the bismuth metal layer on the Sn MPs through chemical reduction and annealing process. The SnBi/a-C MPs were then polymerized with the

dopamine to make SnBi/a-C MPs (see Method Section for details). The schematic illustration of the synthesized process for SnBi/a-C MPs is shown in Figure 2a. A corresponding SEM image of a SnBi/a-C MP as shown in Figure 2b reveals a similar roughness scale as that of Sn/a-C MPs. The average particle size is  $\sim 28.5 \mu\text{m}$  as shown in Figure S1c with the thickness of the carbon layer being  $\sim 303 \text{ nm}$  (Figure S2a). Furthermore, the contrast difference between the core and the shell layer of the SnBi/a-C MP can be observed in the cross-sectional SEM image prepared by FIB (Figure 2c). The EDS line scan solidly confirm the presence of Sn and Bi at the core region, indicating the SnBi alloy as the core material. The strong carbon signal at the shell layer represents that the shell material is pure carbon as shown in Figure 2d (see also Figure S2b). Figure 2e shows XRD spectra of SnBi/a-C and SnBi alloy MPs compared with Sn and Bi metals. The presence of pure Sn and Bi without any metal oxide peaks in the XRD spectra of SnBi confirms the quality of Sn/Bi alloy formation. Moreover, the lack of crystalline carbon peak in XRD spectra of SnBi/a-C MPs indicates the amorphous nature of the carbon layer, which is consistent with the EDS line scan results.

Thermal cycling tests were carried out for the pure Sn, Sn/a-C, and SnBi/a-C MPs by using the DSC for 20 cycles at a ramping rate of  $20 \text{ }^\circ\text{C}/\text{min}$  in the  $\text{Al}_2\text{O}_3$  crucible as shown in Figure 3a, where each cycle consisted of a heating (endothermic) path and a cooling (exothermic) path. The Sn/a-C and SnBi/a-C MPs exhibited the stable latent heats of  $\sim 56$  and  $\sim 45.7 \text{ J/g}$ , respectively, whereas the reduction of latent heat was observed for the pure Sn MPs. The XRD spectra of Sn/a-C and SnBi/a-C MPs before and after the cycling test were shown in Figure 3b,c, respectively. Note that there is no discernible difference before and after the cycling test, which indicates the excellent structural thermal stability of the Sn/a-C and SnBi/a-C MPs. The phase-change processes of the metal and metal alloy core-shell particles have been investigated in our previous works.<sup>15,17</sup> The XRD results in Figure 3a,b confirm the structural stability of the core-shell MPs synthesized in this work, and consequently, the phase change processes of the Sn/a-C and SnBi/a-C core-shell MPs are expected to be similar to those of Sn/SiO<sub>x</sub> and SnZn/SiO<sub>x</sub> core-shell particles, respectively, in our previous works.<sup>15,17</sup> TH is an unfavorable phenomenon for PCMs, which is often observed during a phase-change process. It is well known that substances must be superheated or subcooled to initiate a phase-change process. Here, the TH is defined as the temperature difference between the melting point and the crystallization point of the MPs. In this study, the factors affecting the TH of the MPs were investigated based on our previous work.<sup>27</sup> The thermal resistance of the shell, ramping rate, and heterogeneous nucleation are the three major factors affecting the TH.<sup>27</sup> The heat flow ( $q$ ) in the DSC is negatively correlated with the thermal resistances of the core ( $R_{\text{core}}$ ) and shell material ( $R_{\text{shell}}$ ) as shown in eq 1

Figure 3. (a) Latent heat measurements of SnBi/a-C, Sn/a-C and pure Sn MPs for the 20th cycling. (b) XRD spectra of Sn/a-C MPs after the 20th cycling and the pristine Sn/a-C. (c) XRD spectra of SnBi/a-C MPs after the 20th cycling and the pristine SnBi/a-C.



$$q = \frac{\Delta T_{\text{DSC}}}{R_{\text{core}} + R_{\text{shell}}} \quad (1)$$

where  $\Delta T_{\text{DSC}}$  is the temperature rise in the DSC. Considering one-dimensional heat transfer in the shell,  $R_{\text{shell}}$  can be expressed as [eq 2](#)

$$R_{\text{shell}} = \frac{\delta_t}{(kA)} \quad (2)$$

where  $\delta_t$  is the shell thickness,  $k$  is the thermal conductivity of the shell material, and  $A$  is the area. The latent heat can be defined as total heat absorbed or released by integrating  $q$  with respect to time in the time interval during the phase-change process as shown in [eq 3](#)

$$\text{Latent heat} = \int_{t_i}^{t_f} q \, dt \quad (3)$$

where  $t_i$  and  $t_f$  are the times at the initial state and the final state of the phase-change process. [Figure 4a](#) shows the heat flows of Sn/a-C MPs with different shell thicknesses under a constant ramping rate of 20 °C/min. The inset in [Figure 4a](#) depicts the relations between the shell thicknesses of the Sn/a-C MPs and TH. The TH for Sn/a-C MPs with thicknesses of 0.43, 0.54, and 1.35  $\mu\text{m}$  were  $113 \pm 2$ ,  $113.5 \pm 2$ , and  $115 \pm 2$  °C, respectively. Consequently, the TH is independent of the thickness of the a-C shell layer. For the effect of the ramping rate on the TH, a larger ramping rate led to a more significant heat flow as shown in [eq 1](#). Given a fixed latent heat, a larger heat flow would result in a smaller time interval for the phase-change process according to [eq 3](#). Besides, the temperature difference between the initial state and the final state of the phase-change process is given by [eq 4](#)

$$\Delta T = R \cdot \Delta t \quad (4)$$

where  $R$  is ramping rate and  $\Delta t$  is the time interval of the phase-change process. The temperature difference of the Sn/a-C MPs with a thickness of 0.54  $\mu\text{m}$  under three different ramping rates of 10, 20, and 40 °C/min were 22,

26, and 41°C, respectively (Figure 4b). Despite the smaller  $\Delta t$  obtained under a larger ramping rate; the larger ramping rate accelerated the crystallization process. Therefore, the overall effect of a larger ramping rate is to result in a more significant temperature difference and a larger TH. The heat flows of Sn/a-C MPs with the thickness of 0.54  $\mu\text{m}$  under different ramping rates are shown in Figure 4c. The TH for the ramping rates of 10, 20, and 40 °C/min were 110, 114, and 119 °C, respectively. Moreover, supercooling is needed to initiate the heterogeneous nucleation in the crystallizing process.

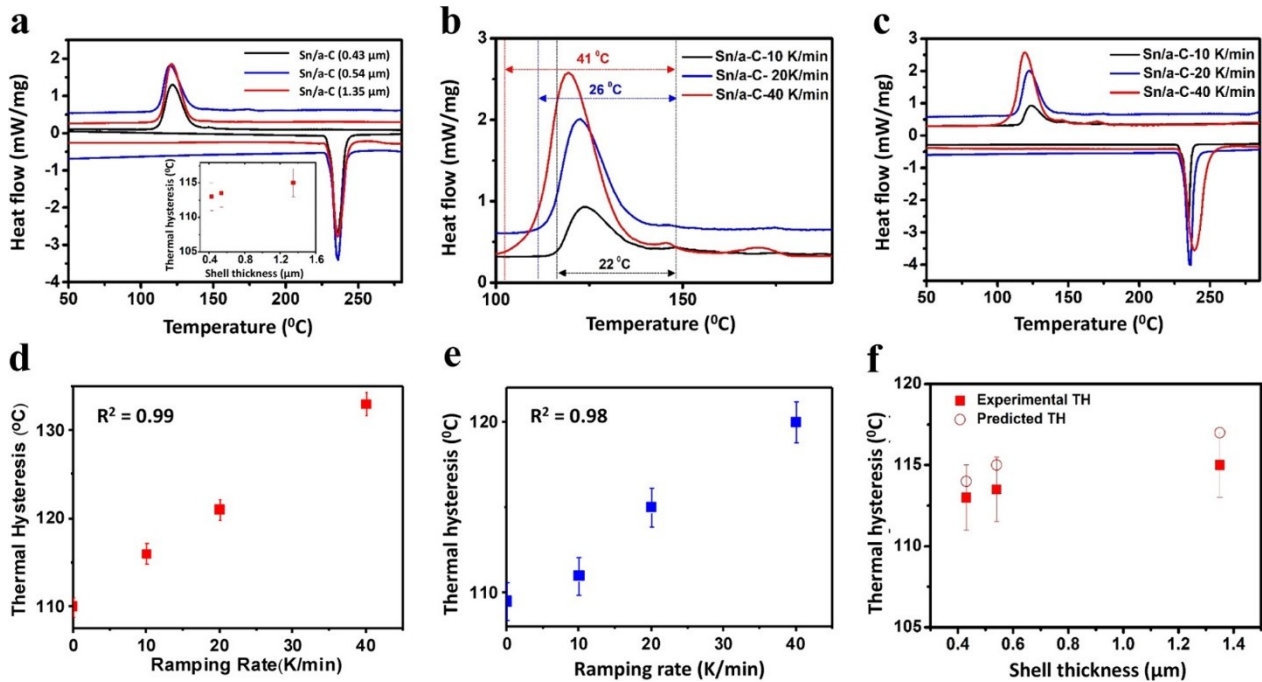


Figure 4. (a) DSC profiles of Sn/a-C MPs with the different shell thicknesses and the TH concerning shell thicknesses of Sn/a-C MPs. (b) Temperature intervals of Sn/a-C MPs concerning different ramping rates. (c) DSC profiles of Sn/a-C MPs with different ramping rates. (d) The influence of heterogeneous nucleation on TH of Sn/a-C MPs. (e) The relations between TH and ramping rate of Sn/a-C MPs. (f) Experimental TH and predicted TH of Sn/a-C MPs.

To investigate the TH due to the heterogeneous nucleation of Sn, the  $\text{Al}_2\text{O}_3$  crucibles used in the DSC were coated by an a-C layer with a thickness of 30 nm. The reason for the a-C coating is to mimic the environment for the heterogeneous nucleation of Sn on the a-C layer, thereby excluding the shell thermal resistance factor on the TH during the melting and crystallization processes. Figure 4d shows the TH under different ramping rates. The TH obtained under the three ramping rates of 10, 20, and 40 °C/min were 116, 121, and 133 °C, respectively. The red dash line is the fitting curve of the experimental data. By extrapolating the fitting curve to the y-axis, the TH resulted from the heterogeneous nucleation alone without incorporating the effect of heating rate could be obtained. The TH resulting from the effect of heterogeneous nucleation was 110 °C. Figure 4e shows the relation between TH and ramping rate where the blue dash line is the fitting line of the experimental data. By extrapolating the fitting line to the y-axis, a TH value of 110 °C can be obtained. The extrapolated TH of 110 °C at a ramping rate of 0 °C/min results from the combined effects of thermal resistance of the shell and heterogeneous nucleation. Consequently, the TH resulting from the shell thermal resistance could be neglected, which is consistent with the

results from [Figure 4a](#) that the TH due to the thermal resistance of shell thickness is minor. From [Figure 4e](#), the difference between the THs obtained at the ramping rate of 20 and 0 K/min for the Sn/a-C MPs with the thickness of 0.54  $\mu\text{m}$  was 5  $^{\circ}\text{C}$ . Therefore, the TH resulted from the giving ramping rate of 20 K/min was 5  $^{\circ}\text{C}$ . The experimental THs under the ramping rate of 20 K/min for shell thicknesses of 0.43, 0.54, and 1.35  $\mu\text{m}$  were  $113 \pm 2$ ,  $113.5 \pm 2$ , and  $115 \pm 2$   $^{\circ}\text{C}$ , respectively, whereas the predicted THs were 114, 115, and 117  $^{\circ}\text{C}$  as shown in [Figure 4f](#). The predicted TH is the summation of THs resulting from the effects of heterogeneous nucleation and the ramping rate at 20 K/min. The predicted values were close to the experimental THs, suggesting that the heterogeneous nucleation and the ramping rate were the two major factors contributing to the TH. After evaluating the factors affecting the TH, it can be concluded that the obtained relatively larger TH of Sn/a-C MPs is mainly due to the required larger superheating and supercooling for heterogeneous nucleation of pure Sn. To decrease the TH and to extend the working temperature range of MPs, Bi was alloyed with Sn and then followed by a coating of an a-C layer to give the SnBi/a-C core-shell MPs. [Figure 5a,b](#) shows the heat flows of SnBi/a-C and Sn/a-C MPs during the thermal cycles in the DSC. The TH of  $\sim 20$   $^{\circ}\text{C}$  for SnBi/a-C MPs was obtained (see [Figure 5a](#)), which is comparatively lower than the TH of  $\sim 110$   $^{\circ}\text{C}$  of Sn/a-C MPs (see [Figure 5b](#)). This is because of the low eutectic point of SnBi alloy (142  $^{\circ}\text{C}$ ) and the low crystallization temperature (120  $^{\circ}\text{C}$ ) of the alloy. Moreover, if the temperature is higher than the eutectic point, the eutectic alloy begins to be melted and forms un-melted Sn clusters. In the subsequent crystallization process, the un-melted Sn clusters act as heterogeneous nucleation sites to promote heterogeneous nucleation, resulting in the reduced TH of SnBi/a-C MPs.

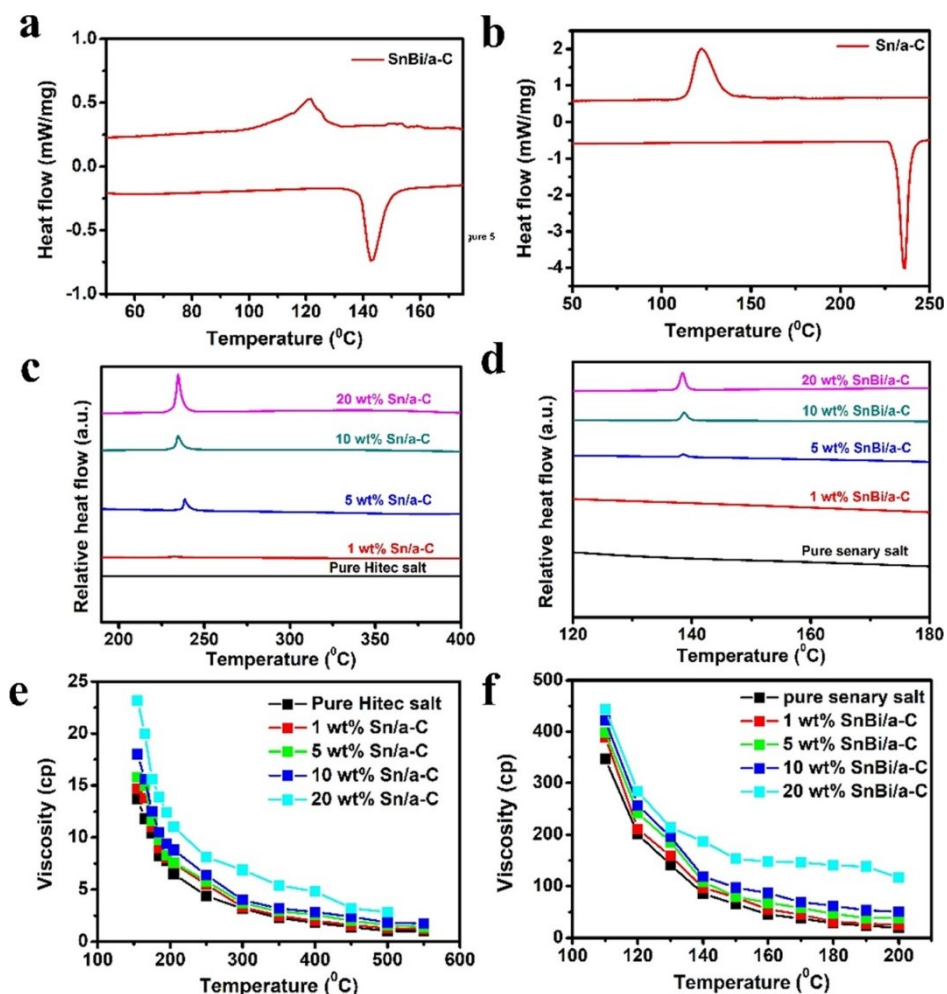


Figure 5. (a,b) DSC profiles of Sn/a-C and SnBi/a-C MPs in a cycle. (c) Heat capacity enhancement results of different wt % of Sn/a-C MPs in commercial molten HITEC salt. (d) Heat capacity enhancement results of different wt % of SnBi/a-C MPs in the nitrate senary salt. (e) Viscosity measurements of different wt % of Sn/a-C MPs in the commercial molten HITEC salt. (f) Viscosity measurements of different wt % of SnBi/a-C MPs in the molten nitrate senary salt.

To evaluate the effectiveness of Sn/a-C MPs in practical applications, the heat capacity of pure HITEC salt doped with Sn/a-C MPs was measured. Compared to the specific heat capacity of the HITEC salt, the specific heat capacities of HITEC salt doped with 1, 5, 10, and 20 wt % of Sn/a-C MPs were enhanced by 2.7, 30, 40, and 200% as shown in Figure 5c, affirming that the specific heat capacity increases with the increase in concentrations of Sn/a-C MPs. The SnBi/a-C MPs have a lower melting point of  $\sim 142$  °C, whereas the HITEC salt's operating temperature range is between 350 and 550 °C. Thus, the nitrate senary molten with a low melting point of  $\sim 75$  °C was also synthesized for the evaluation of the effect of SnBi/a-C MPs on the heat capacity of the salt. The chemical compositions of the as-prepared nitrate senary salt are shown in Table 1. Figure 5d gives the heat flows of pure nitrate senary salt doped with the Sn/a-C MPs.

**Table 1. Chemical Composition of Nitrate Senary Salt**

chemical	purity (%)	content (%)
Ca (NO <sub>3</sub> ) <sub>2</sub> ·4H <sub>2</sub> O	99	23.52
CsNO <sub>3</sub>	99	37.72
K(NO <sub>3</sub> )	99	19.73
Li(NO <sub>3</sub> )	98.5	6.91
Rb(NO <sub>3</sub> )	99.7	6.9
Na(NO <sub>3</sub> )	98	5.22

Compared to the pure senary salt, the specific heat capacities were enhanced by 255, 389, 591, and 734% by doping with 1, 5, 10, and 20 wt % of SnBi/a- C MPs into the salt. Consequently, the Sn/a-C MPs were effective in enhancing the heat capacity of the molten salt. The doping of MPs can also cause an increase in the viscosity of the molten salt, leading to higher energy consumption for a solar thermal power plant. Therefore, the viscosity of the HITEC salt and nitrate senary salt doped with different concentrations of Sn/a-C and SnBi/a-C MPs was investigated. The viscosity of pure HITEC salt decreased from 13.7 to 1.03 cp when temperature increased from 150 to 550 °C as shown in [Figure 5e](#). In addition, the viscosity of the senary salt decreased from 347 to 19 cp as the temperature increased from 110 to 200 °C as shown in [Figure 5f](#). Nevertheless, there is no significant increase in the viscosity for the HITEC salt and molten senary salt by doping with 1, 5, 10, and 20 wt % of Sn/a-C and SnBi/ a-C MPs, respectively, into the salts. Accordingly, the effect of MP doping on the viscosities of the molten salts was not considerable.

To shed light on the practical application of the synthesized MPs, the photo-driven thermal energy effect is investigated. Here, the Sn/a-C MPs as the PCM were chosen for the concept demonstration. The schematic illustration and the photographic images of the solar simulator with and without adding Sn/a-C MPs in the de-ionized (DI) water are shown in [Figure 6a](#). A thermometer was used to measure the temperature variation in the DI water during the solar simulator illumination as shown in [Figure 6a](#). Owing to the broad light absorption ability of the a-C shell layer of the Sn/a- C MPs, a higher temperature increase rate was obtained for the DI water doped with the Sn/ a-C MPs as compared to that for the pure DI water (see [Figure 6b](#)). This result evidenced that the Sn/a-C could be practically applied to enhance energy storage in solar thermal systems.

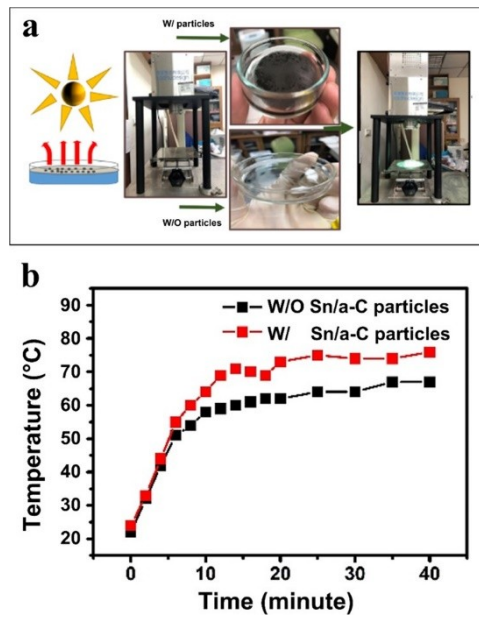


Figure 6. (a) Schematic illustration of photo-driven thermal effect. (b) The relations between temperatures and time for deionization water with and without the Sn/a-C MPs suspension.

#### 4. CONCLUSIONS

In summary, the yolk-shell structure of Sn/a-C MPs with a controllable thickness of the a-C layer on Sn and SnBi MPs have been successfully synthesized. The TH and solar thermal energy storage performance of the MPs were systematically examined. The a-C shell layer acted as a protective layer to prevent oxidation and chemical reactions of the MPs with the salts. A stable latent heat of  $\sim 56$  J/g and a TH of  $\sim 106$  °C were obtained for the Sn/a-C MPs. Furthermore, the SnBi/a-C MPs were synthesized to reduce the TH and a TH of  $\sim 20$  °C was obtained for the SnBi/a-C MPs. The alloying of Bi into Sn MPs plays a major role in reducing the TH. The heat capacities and the viscosities of HITEC salt and senary salt doped with Sn/a-C and SnBi/a-C MPs, respectively, were also examined. The heat capacities were increased by 200 and 734% by doping 20 wt % of Sn/a-C and SnBi/a-C MPs into HITEC and senary salt, respectively. In addition, the effect of particle doping had no significant effect on the viscosities of the HITEC salt and senary salt. Moreover, the DI water doped with Sn/a-C MPs showed an enhanced photo-driven thermal energy effect as compared to the DI water without doping with the MPs.

Consequently, the core-shell particles synthesized in this work are efficient PCMs and they could facilitate the development of solar thermal applications and enhance thermal energy storage in various systems.

## REFERENCES

- (1) World Electricity Generation-World Energy Data. <https://www.worldenergydata.org/world-electricity-generation/> 2021.
- (2) Mitchell, J. F. B. The “Greenhouse” effect and climate change. *Rev. Geophys.* 1989, 27, 115–139.
- (3) Zandalinas, S. I.; Fritschi, F. B.; Mittler, R. Global Warming, Climate Change, and Environmental Pollution: Recipe for a Multifactorial Stress Combination Disaster. *Trends Plant Sci.* 2021, 26, 588–599.
- (4) Araujo, K. The emerging field of energy transitions: Progress, challenges, and opportunities. *Energy Res. Social Sci.* 2014, 1, 112–121.
- (5) Schnitzer, H.; Brunner, C.; Gwehenberger, G. Minimizing greenhouse gas emissions through the application of solar thermal energy in industrial processes. *J. Clean. Prod.* 2007, 15, 1271–1286.
- (6) Forsberg, C. W.; Peterson, P. F.; Zhao, H. High-Temperature Liquid-Fluoride-Salt Closed-Brayton-Cycle Solar Power Towers. *J. Sol. Energy Eng.* 2006, 129, 141–146.
- (7) Milidonis, K.; Blanco, M. J.; Grigoriev, V.; Panagiotou, C. F.; Bonanos, A. M.; Constantinou, M.; Pye, J.; Asselineau, C.-A. Review of application of AI techniques to Solar Tower Systems. *Sol. Energy* 2021, 224, 500–515.
- (8) Steinmann, W.-D.; Tamme, R. Latent Heat Storage for Solar Steam Systems. *J. Sol. Energy Eng.* 2008, 130, 011004.
- (9) Xu, B.; Li, P.; Chan, C. Application of phase change materials for thermal energy storage in concentrated solar thermal power plants: A review to recent developments. *Appl. Energy* 2015, 160, 286–307.
- (10) Yang, Z.; Garimella, S. V. Thermal analysis of solar thermal energy storage in a molten-salt thermocline. *Sol. Energy* 2010, 84, 974–985.
- (11) Hu, R.; Pointer, W. D. CFD Analyses of Natural Circulation in the Air-Cooled Reactor Cavity Cooling System; American Nuclear Society - ANS: United States, 2013.
- (12) Zhang, H. L.; Baeyens, J.; Degreve, J.; Caceres, G. Concentrated solar power plants: Review and design methodology. *Renew. Sustain. Energy Rev.* 2013, 22, 466–481.
- (13) Kenisarin, M. M. High-temperature phase change materials for thermal energy storage. *Renew. Sustain. Energy Rev.* 2010, 14, 955–970.
- (14) Cabeza, L. F.; Castell, A.; Barreneche, C.; de Gracia, A.; Fernández, A. I. Materials used as PCM in thermal energy storage in buildings: A review. *Renew. Sustain. Energy Rev.* 2011, 15, 1675–1695.
- (15) Lai, C.-C.; Chang, W.-C.; Hu, W.-L.; Wang, Z. M.; Lu, M.-C.; Chueh, Y.-L. A solar-thermal energy harvesting scheme: enhanced heat capacity of molten HITEC salt mixed with Sn/SiO<sub>x</sub> core-shell nanoparticles. *Nanoscale* 2014, 6, 4555–4559.

- (16) Cingarapu, S.; Singh, D.; Timofeeva, E. V.; Moravek, M. R. Use of encapsulated zinc particles in a eutectic chloride salt to enhance thermal energy storage capacity for concentrated solar power. *Renewable Energy* 2015, 80, 508–516.
- (17) Lai, C.-C.; Lin, S.-M.; Chu, Y.-D.; Chang, C.-C.; Chueh, Y.-L.; Lu, M.-C. Tunable endothermic plateau for enhancing thermal energy storage obtained using binary metal alloy particles. *Nano Energy* 2016, 25, 218–224.
- (18) Mitran, R.-A.; Ionita, S.; Lincu, D.; Berger, D.; Matei, C. A Review of Composite Phase Change Materials Based on Porous Silica Nanomaterials for Latent Heat Storage Applications. *Molecules* 2021, 26, 241.
- (19) Nomura, T.; Zhu, C.; Sheng, N.; Saito, G.; Akiyama, T. Microencapsulation of Metal-based Phase Change Material for High-temperature Thermal Energy Storage. *Sci. Rep.* 2015, 5, 9117.
- (20) Sharma, A.; Shukla, A.; Chen, C. R.; Wu, T.-N. Development of phase change materials (PCMs) for low temperature energy storage applications. *Sustain. Energy Technol. Assessments* 2014, 7, 17–21.
- (21) Nomura, T.; Sheng, N.; Zhu, C.; Saito, G.; Hanzaki, D.; Hiraki, T.; Akiyama, T. Microencapsulated phase change materials with high heat capacity and high cyclic durability for high-temperature thermal energy storage and transportation. *Appl. Energy* 2017, 188, 9–18.
- (22) Gil, A.; Oró, E.; Miró, L.; Peiró, G.; Ruiz, A.; Salmerón, J. M.; Cabeza, L. F. Experimental analysis of hydroquinone used as phase change material (PCM) to be applied in solar cooling refrigeration. *Int. J. Refrig.* 2014, 39, 95–103.
- (23) Al-Alili, A.; Hwang, Y.; Radermacher, R. Review of solar thermal air conditioning technologies. *Int. J. Refrig.* 2014, 39, 4–22.
- (24) Yuan, K.; Wang, H.; Liu, J.; Fang, X.; Zhang, Z. Novel slurry containing graphene oxide-grafted microencapsulated phase change material with enhanced thermo-physical properties and photo-thermal performance. *Sol. Energy Mater. Sol. Cells* 2015, 143, 29–37.
- (25) Li, K.; Cheng, X.; Li, N.; Zhu, X.; Wei, Y.; Zhai, K.; Wang, H. A yolk/shell strategy for designing hybrid phase change materials for heat management in catalytic reactions. *J. Mater. Chem. A* 2017, 5, 24232–24246.
- (26) Wang, J.; Li, Y.; Deng, L.; Wei, N.; Weng, Y.; Dong, S.; Qi, D.; Qiu, J.; Chen, X.; Wu, T. High-Performance Photothermal Conversion of Narrow-Bandgap Ti<sub>2</sub>O<sub>3</sub> Nanoparticles. *Adv. Mater.* 2017, 29, 1603730.
- (27) Hsu, T.-H.; Chung, C.-H.; Chung, F.-J.; Chang, C.-C.; Lu, M.-C.; Chueh, Y.-L. Thermal hysteresis in phase-change materials: Encapsulated metal alloy core-shell microparticles. *Nano Energy* 2018, 51, 563–570.